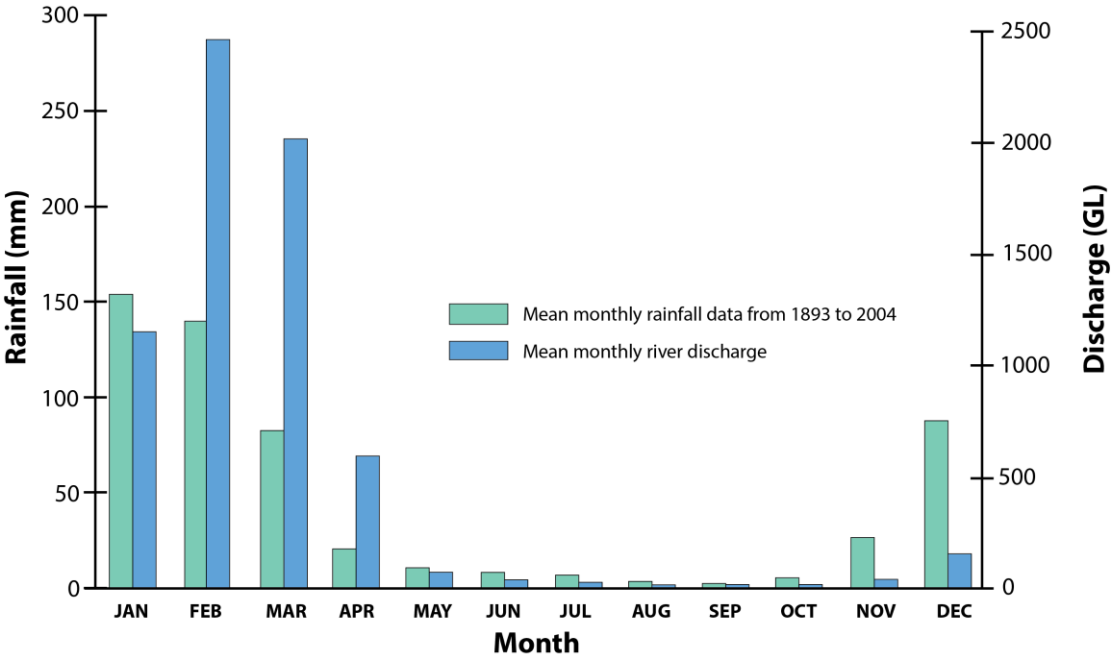

Supplementary Figure 1: Fitzroy River area precipitation and mean monthly river discharge at Fitzroy Crossing (located at 18.11°S/125.33°E, from ref. 1). Sediment discharge, pathways and transport mechanisms across the NW Australian Shelf are complex and influenced by various factors including lateral transport by ocean currents, tidal power, and redeposition by tropical cyclones. However, the fluvial output still remains the determinant factor controlling the temporal distribution of sediments across the NW Australian Shelf[2-4]. Before regulation, the discharge of the main northwestern Australian rivers (Fitzroy and Ord) exhibited an extremely seasonal pattern with more than 90% of fluvial discharge related to summer monsoonal rainfall with extreme flooding events following tropical cyclones[1,5].

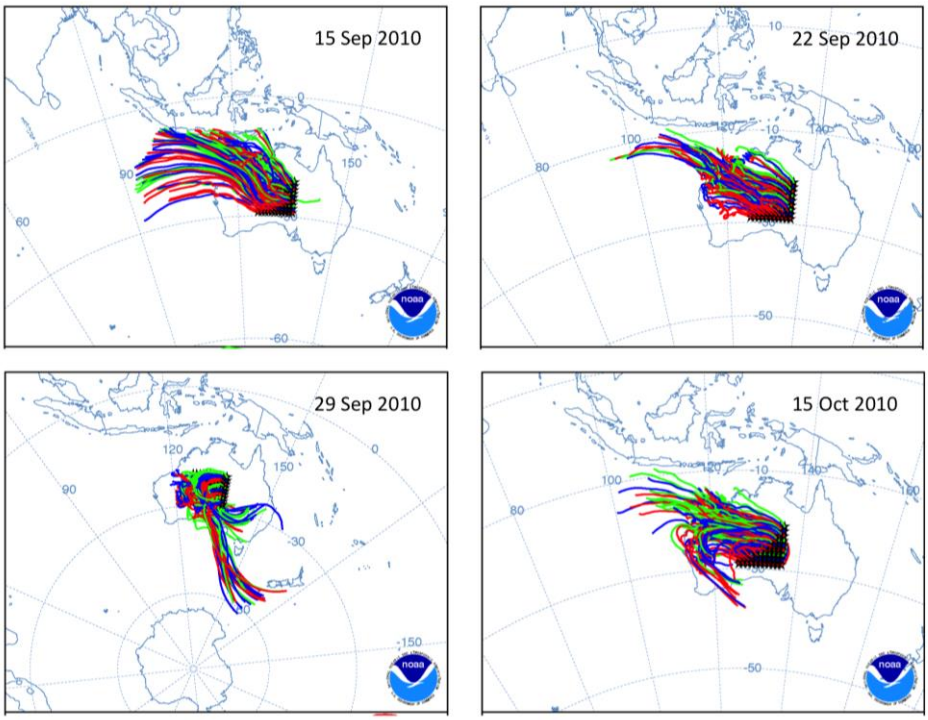

Supplementary Figure 2: Air mass pathways to the Timor Sea. The colored lines show 120 hrs forward trajectory pathway for typical September/October meteorological conditions of dust delivery to the Timor Sea using the HYSPLIT model[6]. The model was set up with GDAS meteorological data and sources at multiple locations in western-central Australia at ground level. The climate and hydrography of the eastern Indian Ocean (Timor Sea) and NW Australia are strongly influenced by seasonal changes in wind direction associated with the southward migration of the ITCZ during austral summer. During December-February, NW winds predominate and rainfall increases over Indonesia and northern Australia (Australian summer monsoon), whereas dry SE trade winds prevail during austral winter in June-November.

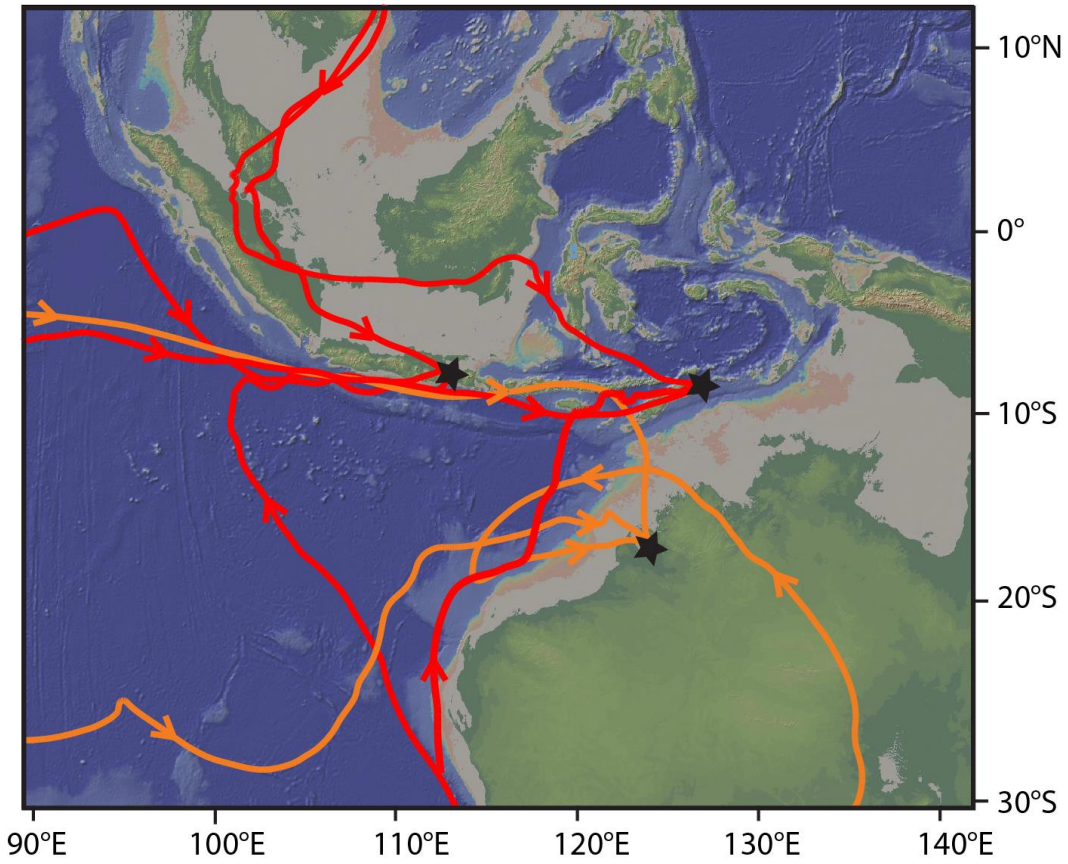

Supplementary Figure 3: Back trajectory air mass pathways for austral summer (January 1st) meteorological conditions using the HYSPLIT model[6]. Model setup uses GDAS meteorological data with source at 500 m above ground level. Stars indicate position of air masses at Jan 1st. Total length of trajectories represent less than 10 days. Red trajectories for Java (years 2011, 2012, 2013) and Timor Leste (years 2007, 2008, 2010) include cross equatorial moisture transport from the South China Sea, while main moisture supply for NW Australia (orange trajectories, years 2010, 2011, 2012) originates in the Southern Hemisphere tropical Indian Ocean. The basemap was generated with GeoMapApp (http://www.geomapapp.org) using the Global Multi-Resolution Topography (GMRT) synthesis database[7]. A distinctive feature triggering the NW Australian monsoon is the formation of low pressure cells over northern Australia between October and December, which precedes the monsoon season by up to three months. The development of these cells plays a critical role in the formation of the Australian summer monsoon circulation, as they trigger strong westerly winds[8]. These heat lows form under clear skies over the desert regions of northern Australia, where surface albedo is high. Their formation, intensity and geographic extent are related to Southern Hemisphere precessional insolation, but are also highly sensitive to obliquity forcing and suborbital variations due to vegetation changes and greenhouse forcing. In contrast to the NW Australian monsoon, the convective rainfall over the Indonesian archipelago is characterized by a pronounced seasonal and regional variability with differing wind patterns and moisture pathways.

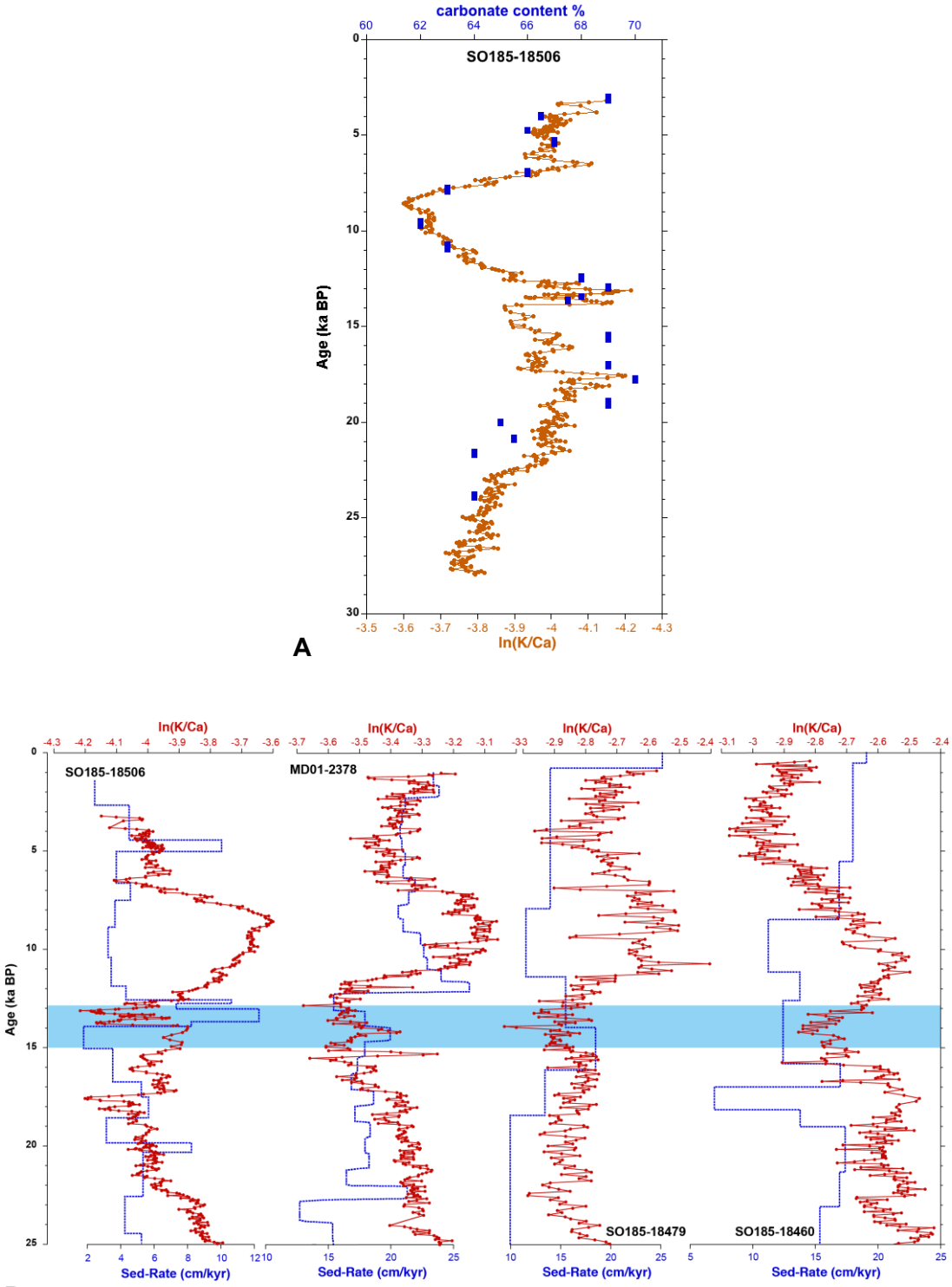

Supplementary Figure 4: Carbonate content (blue squares) and ln(K/Ca) for Core SO185-18506 (**A**). Ln(K/Ca)(red curves) and changes in sedimentation rates (blue dashed lines) for the four cores investigated (**B**). Blue shading indicates the Antarctic Cold Reversal.

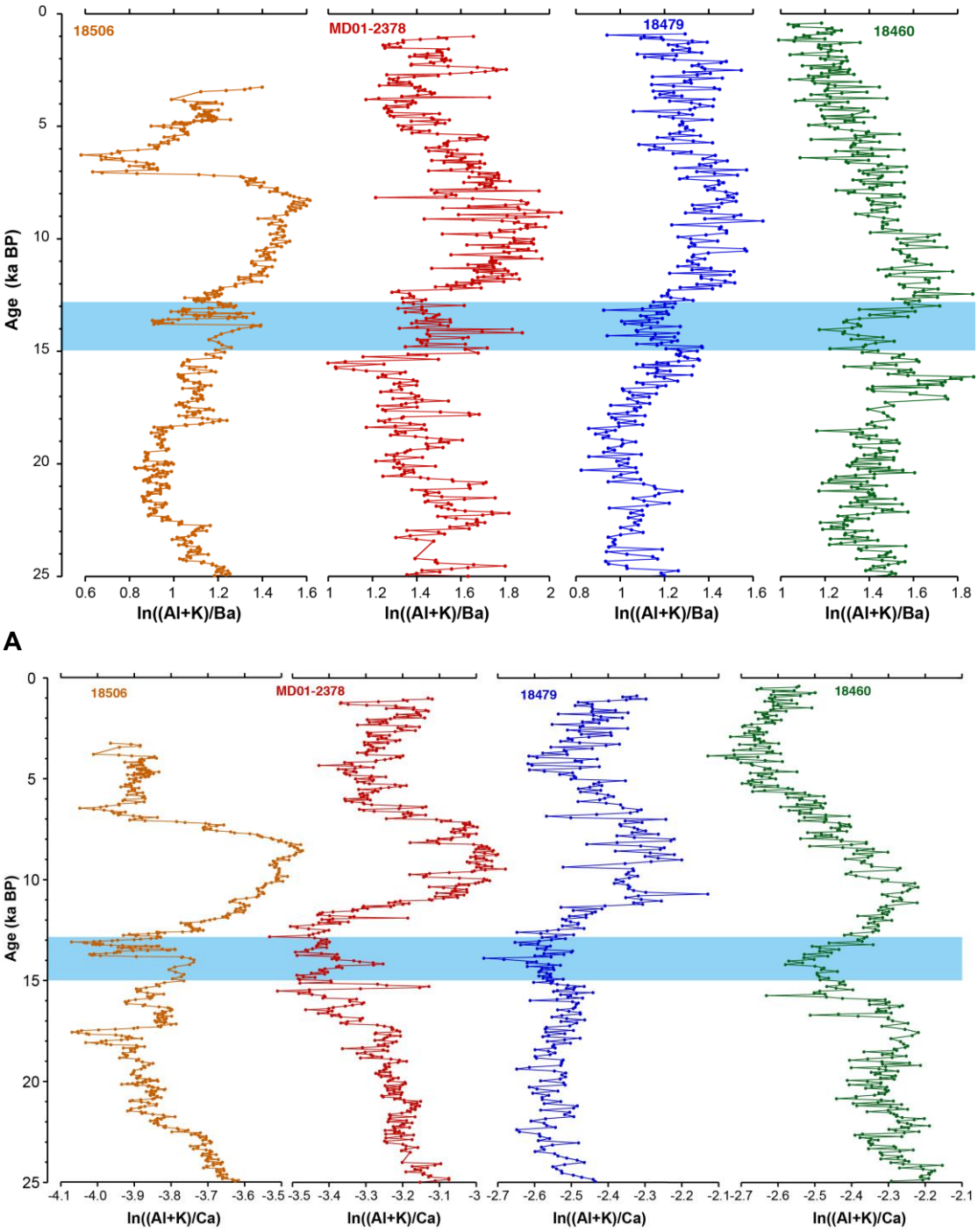

Supplementary Figure 5: (**A**) Ba- and (**B**) Ca-normalized terrigenous elements (Al+K) for the four cores investigated. Blue shading indicates the Antarctic Cold Reversal.

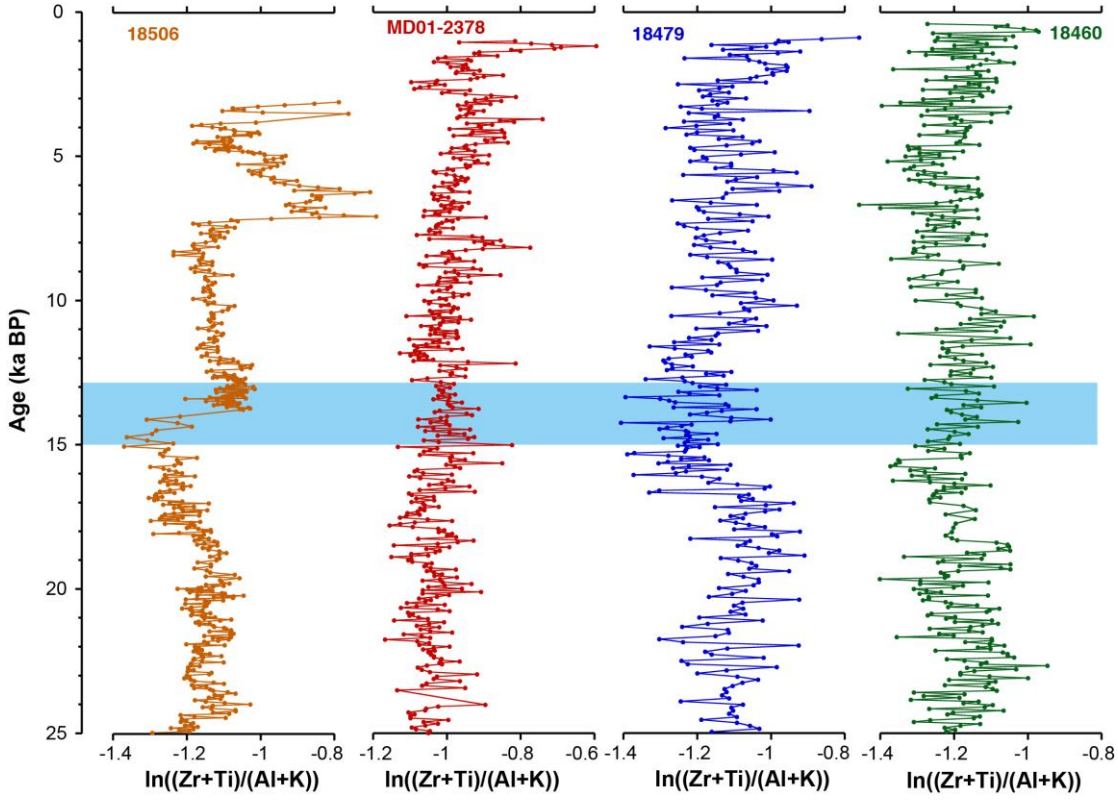
18506
MD01-2378
18479
18460
Age (ka BP)
0
5
10
15
20
25
-1.4
-1.2
-1
-0.8
-0.6
ln((Zr+Ti)/(Al+K))

A

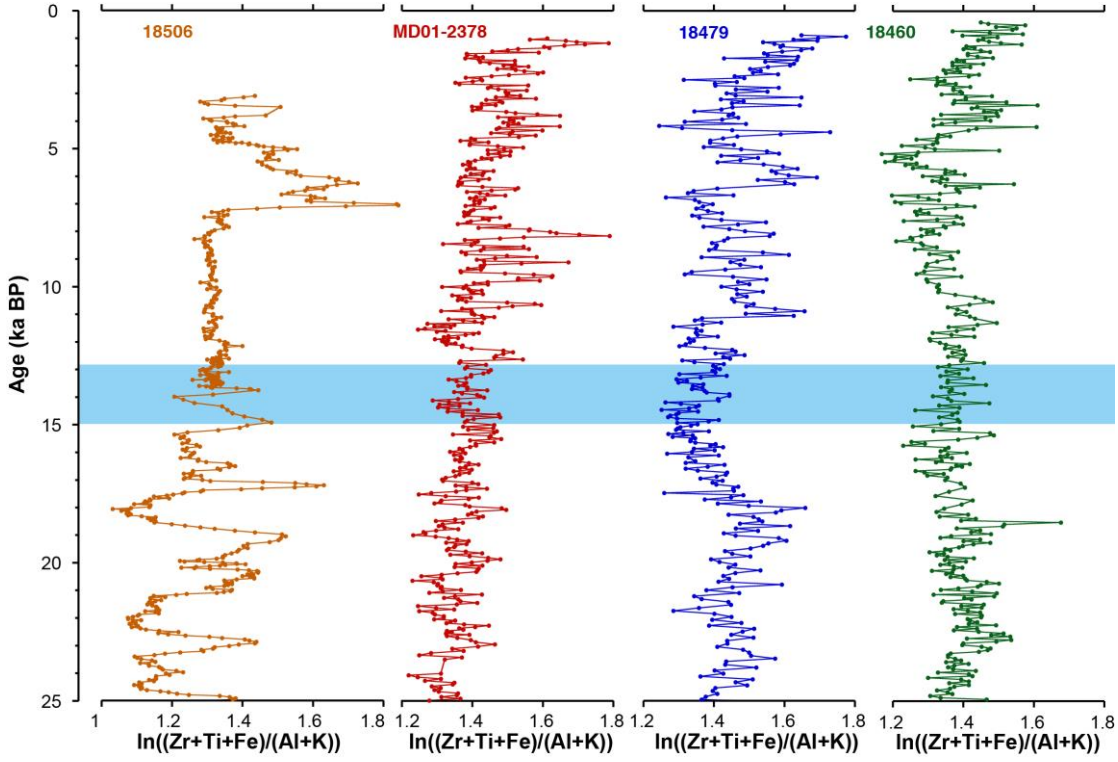
18506
MD01-2378
18479
18460
Age (ka BP)
0
5
10
15
20
25
1
1.2
1.4
1.6
1.8
ln((Zr+Ti+Fe)/(Al+K))

B

Supplementary Figure 6: XRF-scanner proxy data to estimate changes in riverine runoff and aeolian dust: (**A**) ln((Zr+Ti)/(Al+K)) and (**B**) ln((Zr+Ti+Fe)/(Al+K)) in Cores SO185-18596, MD01-2378, SO185-18479 and SO185-18460 versus age along a SW-NE transect. Blue shading indicates the Antarctic Cold Reversal. Estimates of terrigenous dust accumulation off NW Australia range between 1 and 5 g m^{-2} yr^{-1} (ref. 9) which represents ~2-5% of the total sediment mass accumulation or >10% of the terrigenous component at localities in the center of the NW Australian dust belt with typical deglacial sedimentation rates of ~5-10 cm kyr^{-1}. This proportion considerably decreases towards the north, where sedimentation rates increase and dust accumulation decreases, implying that a substantial proportion of the Zr, Ti and Fe content is of aeolian origin only at the southern limit of the area covered by our core transect. The aeolian terrigenous material found in distal marine sediment cores is mostly the outcome of the most extreme dust outbreaks[10]. Increased dust transport to the eastern Indian Ocean may be caused either by soil instability due to reduced vegetation cover during periods of weak austral summer monsoon and/or strengthening in trade wind speed. The occurrence of discrete Zr-, Ti- and Fe-enriched layers in Core SO185-18506 and to a much lesser extent in Cores MD01-2378 and SO185-18479 may, thus, reflect deposition during episodes of enhanced wind strength, similar to recurrent decadal scale dust events observed over West Africa[11]. Core SO185-18460, situated outside the NW Australian dust belt, which mainly receives riverine runoff from nearby Timor and the southern Maluku islands, is characterized by virtually identical ln(K/Ca), ln(Fe/Ca) and ln(Ti/Ca) curves and more constant Zr, Ti and Fe records, when normalized to Al and K. This indicates that the entire terrigenous fraction is derived from riverine runoff, mostly as clay minerals.

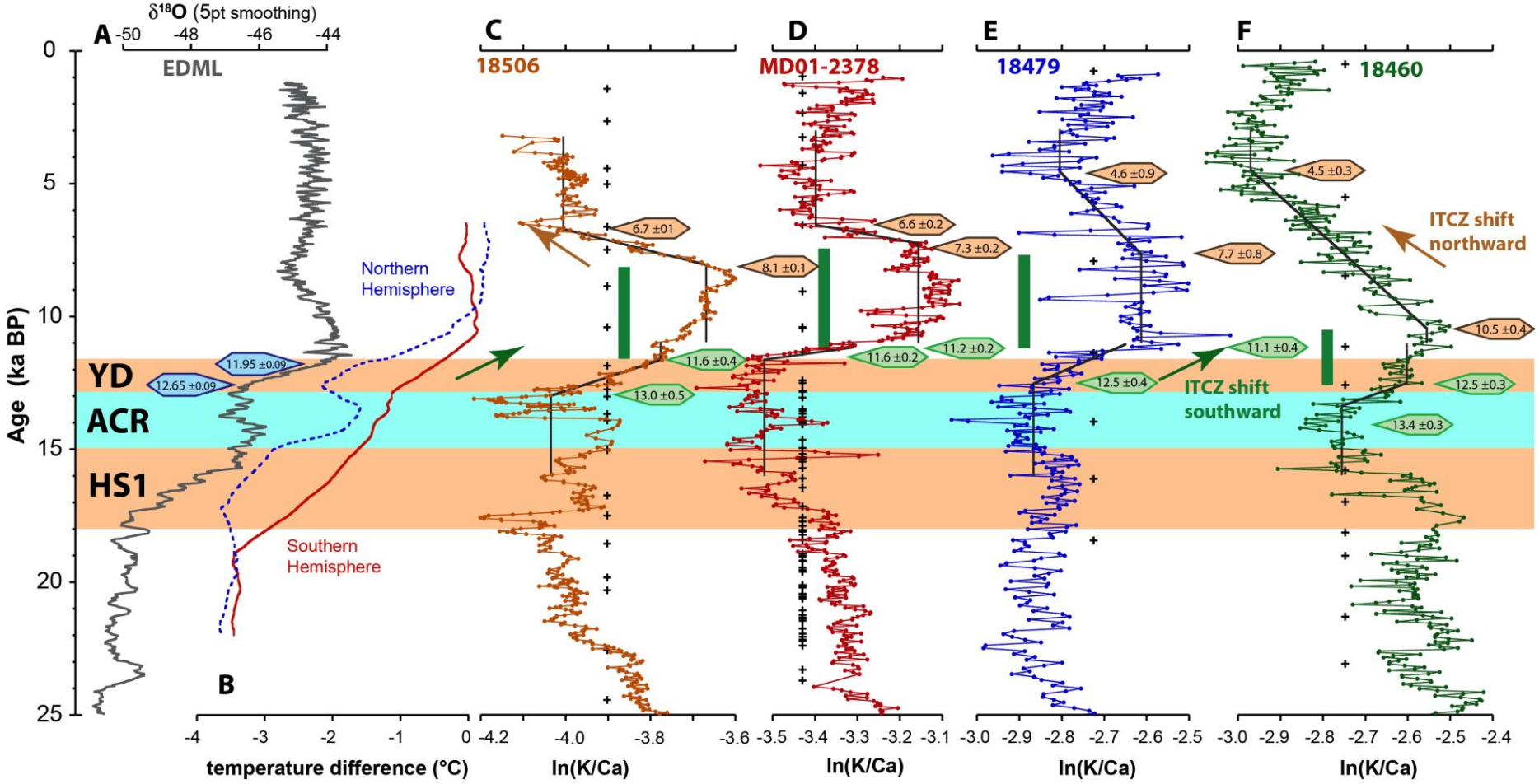
δ18O (5pt smoothing)
A
-50
-48
-46
-44
EDML
0
5
10
15
20
25
Age (ka BP)
YD
ACR
HS1
11.95 ±0.09
12.65 ±0.09
Northern Hemisphere
Southern Hemisphere
B
-4
-3
-2
-1
0
temperature difference (°C)
C
18506
6.7 ±01
11.6 ±0.4
13.0 ±0.5
-4.2
-4.0
-3.8
-3.6
ln(K/Ca)
D
MD01-2378
8.1 ±0.1
6.6 ±0.2
7.3 ±0.2
11.6 ±0.2
11.2 ±0.2
-3.5
-3.4
-3.3
-3.2
-3.1
ln(K/Ca)
E
18479
4.6 ±0.9
7.7 ±0.8
11.1 ±0.4
12.5 ±0.4
ITCZ shift southward
-3.0
-2.9
-2.8
-2.7
-2.6
-2.5
ln(K/Ca)
F
18460
4.5 ±0.3
ITCZ shift northward
10.5 ±0.4
12.5 ±0.3
13.4 ±0.3
-3.0
-2.9
-2.8
-2.7
-2.6
-2.5
-2.4
ln(K/Ca)

Supplementary Figure 7: XRF-scanner riverine runoff proxy records from Cores SO185-18506, MD01-2378, SO185-18479 and SO185-18460 demonstrating monsoonal precipitation increase in NW Australia over the Younger Dryas and earliest Holocene. (**A**) EDML Antarctic ice core $\delta^{18}O_{ice}$ record[12]. (**B**) Northern and Southern Hemisphere temperature stack[13]. (**C**) SO185-18506 (ln(K/Ca)). (**D**) MD01-2378 (ln(K/Ca)). (**E**) SO185-18479 (ln(K/Ca)). (**F**) SO185-18460 (ln(K/Ca)). Green arrows indicate monsoon intensification associated with southward shift of the Intertropical Convergence Zone (ITCZ), brown arrows mark weakening of monsoon associated with northward shift of the ITCZ. Green bars indicate monsoon maxima. Ages in polygons (blue: Antarctic warming; green: Australian Monsoon increase; brown: Australian Monsoon decrease) denote change-points estimated using ramp-regression; error bars (1-sigma) are obtained using 2000 replications from moving block bootstrap resampling[14]. Black crosses indicate ^{14}C AMS dating points. YD = Younger Dryas, ACR = Antarctic Cold Reversal, HS1 = Heinrich Stadial 1.

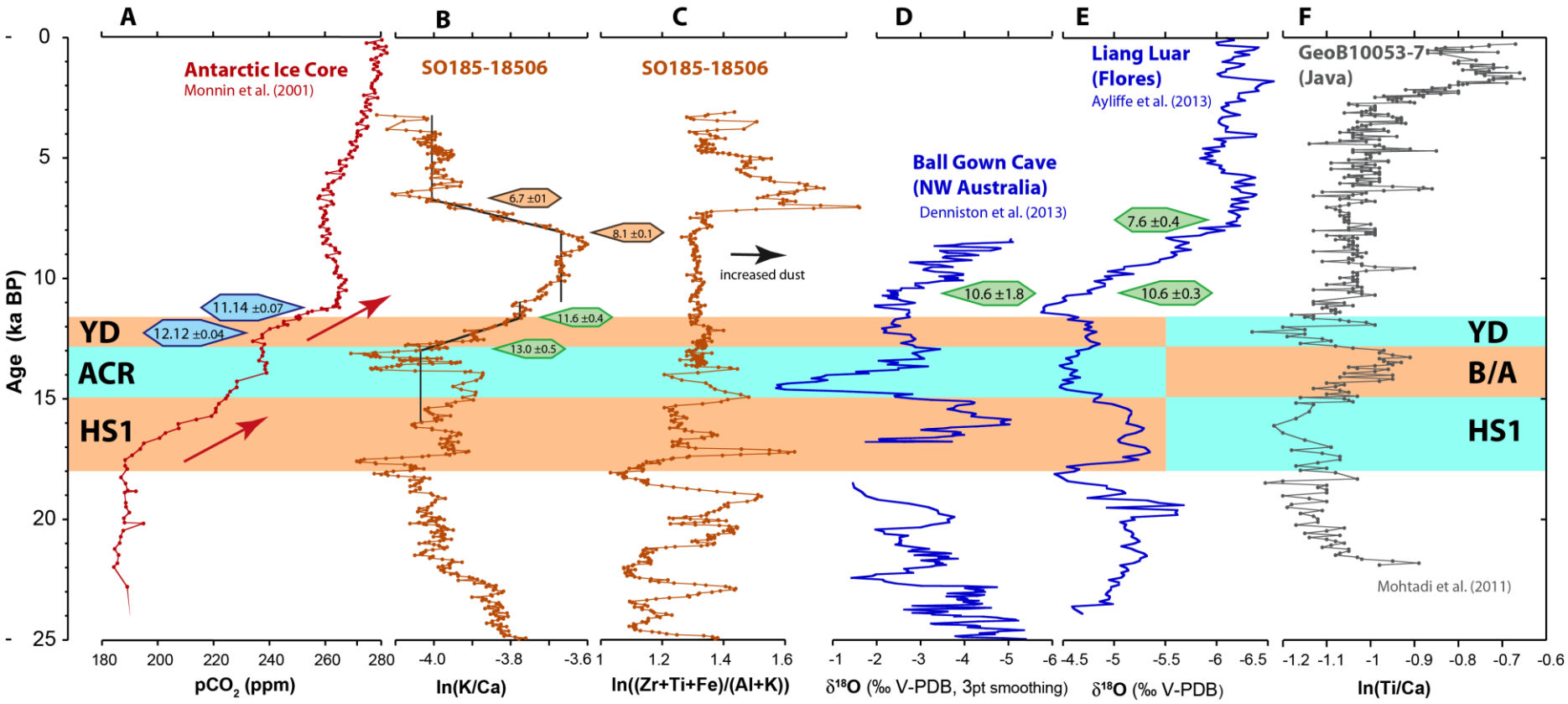
A
B
C
D
E
F
Antarctic Ice Core
Monnin et al. (2001)
SO185-18506
SO185-18506
Ball Gown Cave
(NW Australia)
Denniston et al. (2013)
Liang Luar
(Flores)
Ayliffe et al. (2013)
GeoB10053-7
(Java)
Mohtadi et al. (2011)
Age (ka BP)
YD
ACR
HS1
B/A
11.14 ±0.07
12.12 ±0.04
6.7 ±01
8.1 ±0.1
11.6 ±0.4
13.0 ±0.5
increased dust
10.6 ±1.8
7.6 ±0.4
10.6 ±0.3
pCO2 (ppm)
ln(K/Ca)
ln((Zr+Ti+Fe)/(Al+K))
δ18O (‰ V-PDB, 3pt smoothing)
δ18O (‰ V-PDB)
ln(Ti/Ca)

Supplementary Figure 8: (**A**) Antarctic Ice Core (Dome Concordia) pCO_2 record[15]. (**B**) XRF-scanner derived riverine runoff proxy record from NW Australia from Core SO185-18506. (**C**) XRF scanner-derived NW Australian aeolian dust proxy record from Core SO185-18506. (**D**) NW Australian (Ball Gown Cave) speleothem $\delta^{18}O$ precipitation record[16]. (**E**) Flores (Liang Luar) speleothem $\delta^{18}O$ precipitation record[17]. (**F**) GeoB10053-7 riverine runoff record[18], off South Java. Ages in polygons (blue: CO_2 increase in Antarctic ice core; green: Australian Monsoon increase; brown: Australian Monsoon decrease) denote change-points estimated using ramp-regression; error bars (1-sigma) are obtained using 2000 replications from moving block bootstrap resampling[14]. YD = Younger Dryas, ACR = Antarctic Cold Reversal, HS1 = Heinrich Stadial 1, B/A = Bølling-Allerød.

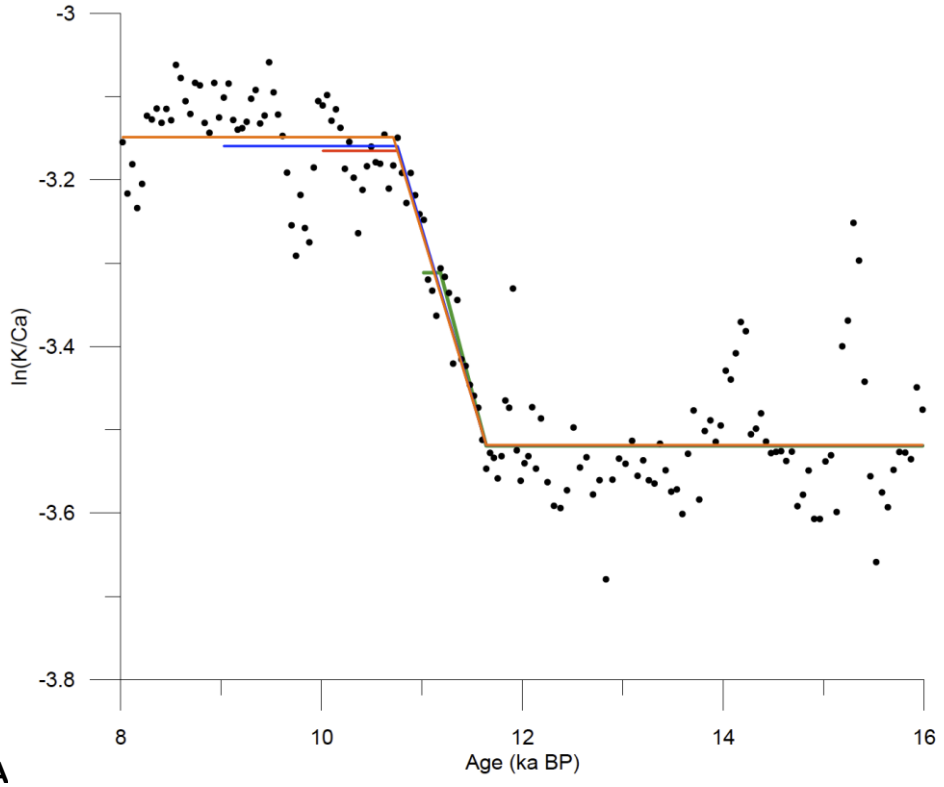
-3
-3.2
-3.4
-3.6
-3.8
ln(K/Ca)
8
10
12
14
16
Age (ka BP)

A

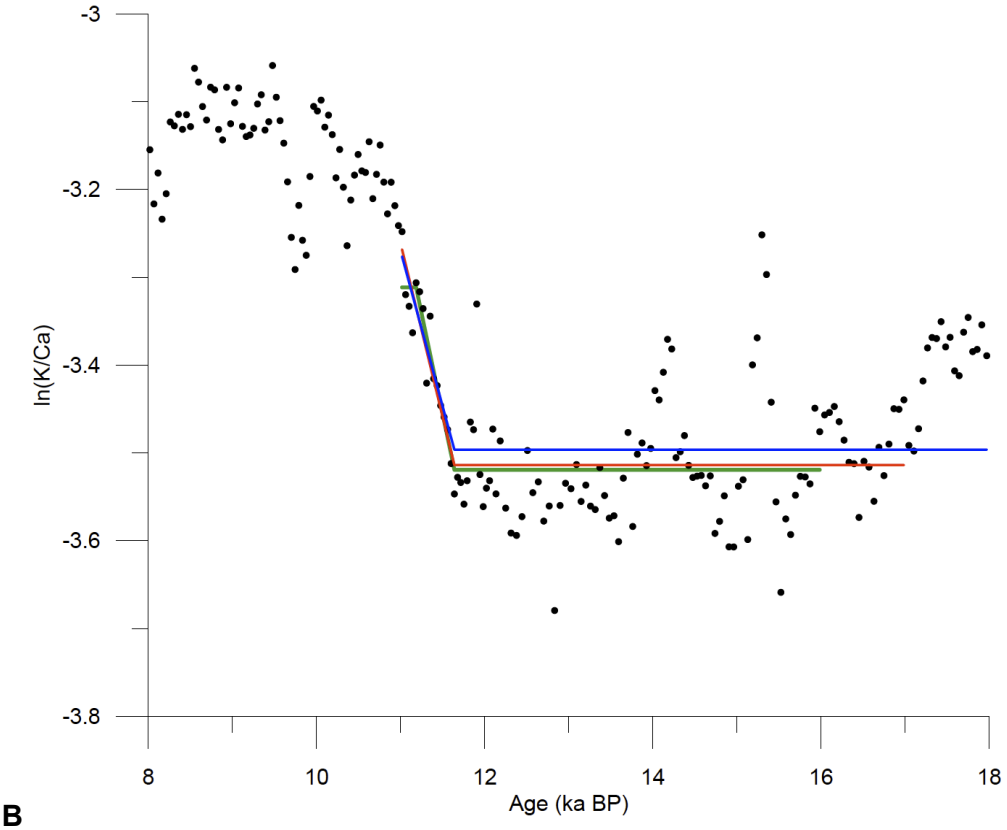
-3
-3.2
-3.4
-3.6
-3.8
ln(K/Ca)
8
10
12
14
16
18
Age (ka BP)

B

Supplementary Figure 9: Sensitivity of the RAMPFIT change-point estimation to the choice of the (**A**) younger (brown = 8 to 16 ka, blue = 9 to 16 ka, red = 10 to 16 ka and green = 11 to 16 ka) and (**B**) older boundary of the fit range. (green = 11 to 16 ka, red = 11 to 17 ka and blue = 11 to 18 ka). In order to evaluate the influence of the fit range on the change-point estimation, we conducted a sensitivity study of the ln(K/Ca) time series in Core MD01-2378, which we re-analyzed with seven different fit-ranges. None of these fit ranges resulted in a change of the onset of the ln(K/Ca) increase at 11.6 ka ± 0.2 ka. Only small changes were observed in the onset of the early Holocene plateau, which is recognized slightly later (10.7 ± 0.2 and 10.8 ± 0.2 instead of 11.2 ± 0.2), when a longer fit range is used.

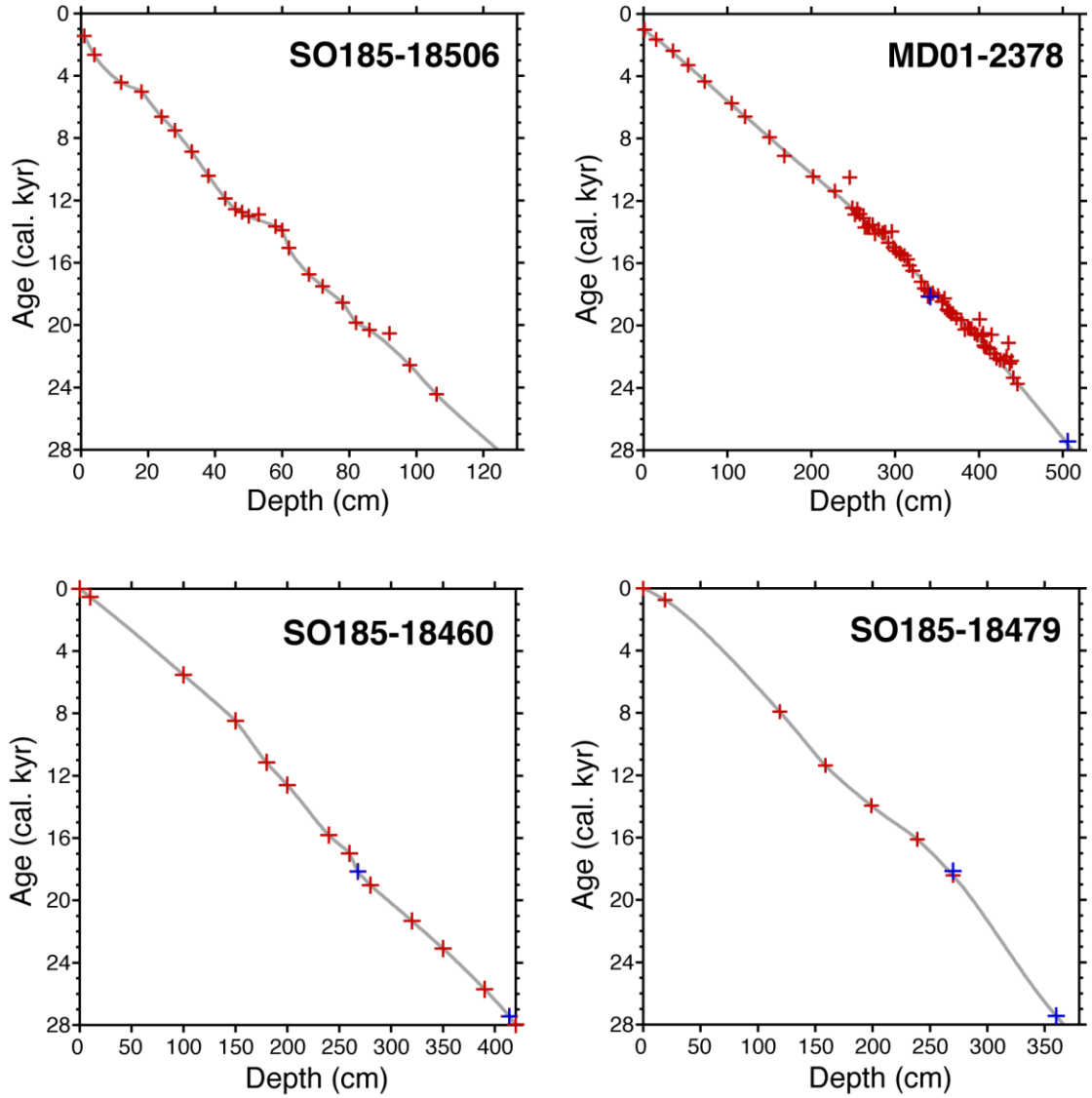

Supplementary Figure 10: Age-depth plots. Core chronologies are based on a total of 114 AMS ^{14}C dates with the addition of two oxygen isotope tiepoints over the LGM part of the record, which were correlated to the EDML (EPICA Dronning Maud Land) ice core δ^{18}O record, recovered from Antarctica[12]. This ice core has been synchronized to the layer-counted NGRIP (North Greenland Ice Core Project) ice core following the new Greenland Ice Core Chronology (GICC05) timescale[12, 19]. We used the Stineman function in Kaleidagraph for interpolation between age tiepoints. For Cores SO185-18506, SO185-18479 and SO185-18460, we used an interpolate function that forces the interpolation through the tiepoints. For Core MD01-2378, which is based on 76 AMS dates, we preferred a smooth interpolation, which avoids artificial age-changes at ^{14}C plateaus[20]. Tiepoints based on benthic δ^{18}O correlation to the EDML ice core δ^{18}O record are indicated with blue crosses. We did not use the AMS date at 53 cm in Core SO185-18506, which yielded a slightly too young age (12.896 ka BP) due to bioturbational effects associated with a redox boundary at this position, and the date at 20.529 ka BP in Core SO185-18506, which corresponds to one of the ^{14}C plateaus recognized in Core MD01-2378.

Supplementary Table 1: Statistical change point estimates using RAMPFIT[21].

	Lower fitted change point (interval 3–11 ka) onset of drying after monsoon maximum	value (ln(K/Ca)), $\delta^{18}O$	Upper fitted change point (interval 3–11 ka) end of drying	value (ln(K/Ca)), $\delta^{18}O$	Lower fitted change point (interval 11–16 ka)* onset of monsoon/warming/CO_2 increase	value (ln(K/Ca)), $\delta^{18}O$, ppm	Upper fitted change point (interval 11–16 ka) beginnig of monsoon maximum/end of warming/CO_2 increase	value (ln(K/Ca)), $\delta^{18}O$, ppm
SO185-18460	**10.5**	-2.55	**4.5**	-2.97	**13.4**	-2.76	**12.5**	-2.60
± ****	0.4	0.02	0.3	0.01	0.3	0.01	0.3	0.01
SO185-18479	**7.7**	-2.61	**4.6**	-2.81	**12.5**	-2.87	**11.1****	-2.65
±****	0.8	0.02	0.9	0.03	0.4	0.01	0.4	0.04
MD01-2378	**7.3**	-3.16	**6.6**	-3.40	**11.6**	-3.52	**11.2****	-3.31
±****	0.2	0.01	0.2	0.01	0.2	0.01	0.2	0.06
SO185-18506	**8.1**	-3.67	**6.7**	-4.01	**13.0**	-4.04	**11.6**	-3.78
± ****	0.1	0.01	0.1	0.01	0.5	0.03	0.4	0.04
Ball Gown					**10.6**	-2.7	**8.4****	-4.6
± ****					1.8	0.5	1.7	0.7
Liang Luar					**10.6**	-4.71	**7.6**	-6.14
± ****					0.3	0.05	0.4	0.06
EDML $\delta^{18}O$					**12.65**	-46.47	**11.95**	-43.9
±****					0.09	0.06	0.09	0.1
EDML CO_2					**12.12*****	238.3	**11.14*****	264
± ****					0.04	0.5	0.07	1.0

* interval 11–14 ka for Core SO185-18506 and EDML CO_2, interval 8.4–16 ka for Ball Gown Cave and interval 3–16 ka for Liang Luar (longer fit interval was required to obtain interpretable results).

** estimate close to fit interval boundary.

*** shorter fit interval allows to quantify this shorter-term change at ~12–11 ka.

**** 1-sigma error.

Supplementary Table 2: AMS ^{14}C dates.

Core	Depth	^{14}C age	^{14}C age res. Corr.	stdev	Cal. age BP	stdev
SO185-18460	10	905	505	25	524	10
SO185-18460	100	5170	4770	35	5524	55
SO185-18460	150	8105	7705	50	8481	53
SO185-18460	180	10105	9705	55	11148	77
SO185-18460	200	11050	10650	50	12600	52
SO185-18460	240	13990	13590	70	15819	134
SO185-18460	260	14820	14420	90	16996	190
SO185-18460	280	16260	15860	100	19020	115
SO185-18460	320	18370	17970	100	21321	170
SO185-18460	350	19800	19400	120	23092	217
SO185-18460	390	21810	21410	150	25696	240
SO185-18460	420	23720	23320	190	27969	256
SO185-18479	19	1255	855	30	755	35
SO185-18479	119	7480	7080	45	7916	42
SO185-18479	159	10365	9965	60	11379	123
SO185-18479	199	12570	12170	70	13957	86
SO185-18479	239	14240	13840	90	16119	158
SO185-18479	270	15590	15190	90	18424	145
SO185-18506	1	1950	1550	60	1432	68
SO185-18506	4	2920	2520	25	2657	75
SO185-18506	12	4370	3970	30	4430	34
SO185-18506	18	4830	4430	30	5027	85
SO185-18506	24	6215	5815	30	6629	39
SO185-18506	28	7015	6615	35	7501	35
SO185-18506	33	8380	7980	45	8868	112
SO185-18506	38	9640	9240	45	10410	83
SO185-18506	43	10575	10175	55	11866	120
SO185-18506	46	11005	10605	45	12562	52
SO185-18506	48	11245	10845	50	12750	51
SO185-18506	50	11580	11180	55	13023	56
SO185-18506	53	11425	11025	60	12896	59
SO185-18506	58	12225	11825	60	13674	63
SO185-18506	60	12530	12130	55	13917	70
SO185-18506	62	13310	12910	110	15040	155
SO185-18506	68	14660	14260	80	16741	152
SO185-18506	72	15100	14700	80	17505	211
SO185-18506	78	15720	15320	90	18563	100
SO185-18506	82	17100	16700	100	19834	131
SO185-18506	86	17540	17140	120	20319	122
SO185-18506	92	17760	17360	100	20529	124
SO185-18506	98	19390	18990	120	22566	139
SO185-18506	106	20930	20530	130	24447	172

Core	Depth	^{14}C age	^{14}C age res. Corr.	stdev	Cal. age BP	stdev
MD01-2378	1	1515	1115	30	1011	37
MD01-2378	15	2130	1730	40	1637	56
MD01-2378	35	2780	2380	40	2379	62
MD01-2378	53	3465	3065	35	3291	49
MD01-2378	73	4295	3895	30	4341	59
MD01-2378	105	5405	5005	35	5733	57
MD01-2378	121	6190	5790	35	6595	52
MD01-2378	150	7485	7085	45	7920	41
MD01-2378	168	8575	8175	40	9106	65
MD01-2378	202	9660	9260	45	10444	79
MD01-2378	228	10370	9970	50	11381	109
MD01-2378	246	9690	9290	45	10489	67
MD01-2378	249	10905	10505	55	12454	84
MD01-2378	252	11415	11015	50	12887	52
MD01-2378	255	10995	10595	55	12552	61
MD01-2378	258	11375	10975	50	12854	53
MD01-2378	262	11670	11270	50	13104	62
MD01-2378	264	12260	11860	80	13701	77
MD01-2378	267	12260	11860	70	13702	70
MD01-2378	269	12150	11750	55	13609	64
MD01-2378	273	12080	11680	55	13544	68
MD01-2378	276	12705	12305	55	14110	96
MD01-2378	280	12430	12030	60	13834	64
MD01-2378	285	12660	12260	58	14054	89
MD01-2378	288	12610	12210	55	13996	79
MD01-2378	292	13020	12620	55	14694	106
MD01-2378	296	12580	12180	60	13966	80
MD01-2378	298	13270	12870	60	14995	111
MD01-2378	301	13470	13070	60	15223	120
MD01-2378	305	13580	13180	65	15349	126
MD01-2378	307	13640	13240	70	15418	131
MD01-2378	311	13725	13325	65	15515	129
MD01-2378	315	13940	13540	60	15761	127
MD01-2378	317	14260	13860	70	16144	141
MD01-2378	321	14500	14100	70	16486	152
MD01-2378	331	14930	14530	85	17192	208
MD01-2378	335	15160	14760	70	17621	200
MD01-2378	339	15230	14830	75	17762	208
MD01-2378	339	15410	15010	70	18126	193
MD01-2378	345	15310	14910	70	17925	198
MD01-2378	351	15390	14990	80	18086	208
MD01-2378	356	15625	15225	80	18470	115
MD01-2378	359	15480	15080	80	18258	185
MD01-2378	362	16210	15810	80	18979	100
MD01-2378	364	16310	15910	80	19061	104
MD01-2378	365	16340	15940	80	19086	104
MD01-2378	367	16530	16130	90	19259	114
MD01-2378	369	16500	16100	80	19230	107
MD01-2378	373	16790	16390	80	19505	97
MD01-2378	379	16950	16550	90	19666	114
MD01-2378	383	17470	17070	90	20256	97

Core	Depth	^{14}C age	^{14}C age res. Corr.	stdev	Cal. age BP	stdev
MD01-2378	387	17370	16970	80	20160	101
MD01-2378	389	17410	17010	95	20199	110
MD01-2378	391	17440	17040	90	20228	100
MD01-2378	395	17740	17340	90	20507	112
MD01-2378	398	17830	17430	90	20606	125
MD01-2378	401	16880	16480	80	19593	97
MD01-2378	403	17890	17490	90	20677	132
MD01-2378	405	17725	17325	100	20492	119
MD01-2378	406	18340	17940	140	21282	220
MD01-2378	407	18410	18010	110	21380	186
MD01-2378	409	18440	18040	90	21422	162
MD01-2378	413	18490	18090	100	21500	180
MD01-2378	415	17820	17420	100	20595	134
MD01-2378	418	18670	18270	110	21799	199
MD01-2378	421	18890	18490	120	22107	151
MD01-2378	425	18990	18590	100	22212	112
MD01-2378	430	19050	18650	100	22264	108
MD01-2378	433	18790	18390	110	21985	170
MD01-2378	435	18220	17820	110	21112	176
MD01-2378	437	19260	18860	110	22441	116
MD01-2378	439	19060	18660	100	22272	105
MD01-2378	441	19960	19560	110	23352	189
MD01-2378	446	20280	19880	120	23755	164
MD01-2378	592	29920	29520	330	34938	354

Supplementary Table 3: Benthic oxygen isotope age tiepoints in Cores SO185-18460, SO185-18479, and MD01-2378: 1) $\delta^{18}O$ maximum prior to deglaciation and 2) $\delta^{18}O$ maximum after AIM4 event.

Tiepoint		1	2
Age (ka)		18.15	27.45
SO185-18460	depth (cm)	268	414
SO185-18479	depth (cm)	270	360
MD01-2378	depth (cm)	342	506

Supplementary Note 1: Core locations and recovered sedimentary records

The area encompassing the Timor Strait and NW Australia is ideally suited to test model predictions of a Southern (Northern) Hemisphere temperature forcing of the Indonesian-Australian Monsoon, since sedimentation patterns in the Timor Sea are directly related to latitudinal migrations of the austral summer monsoon rain belt. Intensified and prolonged summer monsoon rainfall over NW Australia during southward shifts of the austral summer Intertropical Convergence Zone (ITCZ) increases the load transport of the Fitzroy and Ord Rivers, leading to enhanced deposition of terrigenous sediment of fluvial origin along the NW Australian continental margin. In contrast, the austral summer monsoon weakens, vast areas of northern Australia dry out and intense trade winds carry increased amounts of dust from the continent into the SE Timor Sea, when the ITCZ is locked into a more northerly position.

We examine the riverine runoff and dust flux patterns at four strategically positioned core locations forming a SW-NE transect from the NW Australian "dust belt" across the southern limit of intense Australian summer monsoon rainfall into the center of tropical convective rain offshore Timor Leste.

Piston-Core SO185-18460 (8° 47.386' S, 128° 38.485' E; 1875 m water depth, Fig. 1) was recovered at the tip of an elevated promontory at the northern flank of the Timor Trough, east of Timor Leste, below the main flow of the Indonesian Throughflow (ITF) through the Timor Strait[22]. The core consists of undisturbed, homogenous, nannoplankton ooze with high clay content, abundant planktonic foraminifers and relatively rare benthic foraminifers. Sedimentation rates range between 10 and 18 cmkyr^{-1} across the last glacial termination.

Piston-Core SO185-18479 (12°27.159'S, 121° 22.395'E, 2974 m water depth, Fig. 1) is located ~100 nautical miles west of the Ashmore Reef and close to the main ITF outflow from the Timor Strait. Sediment composition and sedimentation rates are quite similar to that in Core SO185-18460.

IMAGES Calypso-Core MD01-2378 (13˚4.95´S, 121˚47.27´E; water depth: 1783 m, Fig. 1) was recovered in the Timor Sea at the northwestern margin of the Scott Plateau[23]. The core is situated slightly south of the ITF main outflow pathway and to the north of the main dust belt transported from the NW Australian desert into the Timor Sea by trade winds during austral winter[24]. The sediment consists of undisturbed, homogenous, nannoplankton ooze with 50 to 55% carbonate. Sedimentation rates of ~10 cm kyr^{-1} over the late Pleistocene[25] are somewhat lower than at Sites SO185-18460 and SO185-18479.

Piston-Core SO185-18506 (15°18.656'S, 119° 30.052'E, water depth 2410 m, Fig. 1), recovered ~200 nautical miles SSE of the Scott Reef, represents the southwest end of our core transect. It is situated at the northern margin of the NW Australian dust belt[24]. The core consists of pelagic nannoplankton ooze with abundant planktonic foraminifers with smaller amounts of land-derived clay than in other cores. The carbonate content varies between 62 and 72 % and the average sedimentation rate is only ~5 cm kyr^{-1}.

Supplementary references

1. Lindsay, R.P., and Commander, D.P. Hydrological Assessment of the Fitzroy Alluvium. Government of Western Australia, Department of Water Report N°. HG16, 41 pp (2006).
2. Glenn, K. Sedimentary processes during the Late Quaternary across the Kimberley Shelf, Northwest Australia. PhD Thesis University of Adelaide, Department of Geology and Geophysics, 245 pp (2004).
3. Margvelashvili, N., Andrewartha, J., Condie, S., Herzfeld, M., Parslow, J., Sakov, P., and Waring, J. Modelling suspended sediment transport on Australia's North West Shelf. Northwest Shelf Joint Environmental Management Study, Technical Report N°7, 43 pp (2006).
4. Alongi, D.M., da Silva, M., Wasson, R.J., and Wirasantosa, S. Sediment discharge and export of fluvial carbon and nutrients into the Arafura and Timor Seas: A regional synthesis. *Marine Geology* **343**, 146-158 (2013). http://dx.doi.org/10.1016/j.margeo.2013.07.004
5. Doupé, R.G., and Pettit, N.E. Ecological perspectives on regulation and water allocation for the Ord River, Western Australia. *River Research and Applications* **18**, 307-320, doi:10.1002/rra.676 (2002).
6. Draxler, R.R., and Rolph, G.D. HYSPLIT (HYbrid Single-Particle Lagrangian Integrated Trajectory) Model access via NOAA ARL READY Website (http://ready.arl.noaa.gov/HYSPLIT.php). NOAA Air Resources Laboratory, Silver Spring, MD (2013).
7. Ryan, W.B.F., Carbotte, S.M., Coplan, J.O., O'Hara, S., Melkonian, A., Arko, R., Weissel, R.A., Ferrini, V., Goodwillie, A., Nitsche, F., Bonczkowski, J., and Zemsky, R. Global Multi-Resolution Topography synthesis, Geochemistry Geophysics Geosystems, **10**, Q03014, doi:10.1029/2008GC002332 (2009).
8. Suppiah, R. The Australian summer monsoon: a review. *Progress in Physical Geography* **16**, 283-318 (1992).
9. Jickells, T., An, Z. S., Andersen, K.K., Baker, A.R., Bergametti, G., Brooks, N., Cao, J.J., Boyd, P., Duce, R., Hunter, K.A., Nilgün Kubilay , LaRoche, J., Liss P., Mahowald, P.S., Prospero, J.M., Ridgwell, A.J., Tegen, I., and Torres, R. Global iron connections between desert dust, ocean biogeochemistry, and climate. *Science* **308**, 67-71 (2005).
10. Rea, D.K. The paleoclimatic record provided by eolian deposition in the deep sea: the geologic history of wind. *Review of Geophysics* **32**, 159-195 (1994).
11. Hanebuth, T., and Henrich, R. Recurrent decadal-scale dust events over Holocene western Africa and their control on canyon turbidite activity (Mauritania). *Quaternary Science Reviews* **28**, 261-270 (2009).
12. EPICA Community members. One-to-one coupling of glacial climate variability in Greenland and Antarctica. *Nature* **444**, 195-198 (2006).
13. Shakun, J.D., Clark, P.U., He, F., Marcott, S.A., Mix, A.C., Liu, Z., Otto-Bliesner, B., Schmittner, A., and Bard, E. Global warming preceded by increasing carbon dioxide concentrations during the last deglaciation. *Nature* **484** (7392), 49-54, doi:10.1038/nature10915 (2012).
14. Mudelsee, M. Climate Time Series Analysis: Classical Statistical and Bootstrap Methods. Springer, Dordrecht, 474 pp (2010).
15. Monnin, E., Indermühle, A., Dällenbach, A., Flückiger, J., Stauffer, B., Stocker, T.F., Raynaud, D., and Barnola, J.-M. Atmospheric CO_2 concentrations over the last glacial termination. *Science* **291** (5501), 112-114 (2001).
16. Denniston, R.F., Wyrwoll, K.-H., Asmerom, Y., Polyak, V.J., Humphreys, W.F., Cugley, J., Woods, D., LaPointe, Z., Peota, J., and Greaves, E. North Atlantic forcing of millennial-scale Indo-Australian monsoon dynamics during the Last Glacial period. *Quaternary Science Reviews* **72,** 159-168 http://dx.doi.org/

10.1016/j.quascirev.2013.04.012 (2013).
17. Ayliffe, L.K., Gagan, Michael, K., Zhao, J-X., Drysdale, R., Hellstrom, J.C., Hantoro, A.S., Griffiths, M.L., Scott-Gagan, H., Pierre, E.S., Cowley, J.A., and Suwargardi, B.W. Rapid interhemispheric climate links via the Australasian monsoon during the last deglaciation. *Nature Communications* http://dx.doi.org/10.1038/ncomms3908 (2013).
18. Mohtadi, M., Oppo, D.W., Steinke, S., Stuut, J.-B., W., De Pol-Holz, R., Hebbeln, D., and Lückge, A. Glacial to Holocene swings of the Australian-Indonesian monsoon. *Nature Geoscience* **4**, 540-544, doi:10.1038/NGEO1209 (2011).
19. Andersen, K.K., Svensson, A., Johnsen, S.J., Rasmussen, S.O., Bigler, M., Röthlisberger, R., Ruth, U., Siggaard-Andersen, M.-L., Steffensen, J.P., Dahl-Jensen, D., Vinther, B.M., Clausen, H.B., et al. The Greenland ice core chronology 2005, 15-42 ka. Part 1: Constructing the time scale. *Quaternary Science Reviews* **25**, 3246-3257 (2006).
20. Sarnthein, M., Grootes, P.M., Holbourn, A., Kuhnt, W., and Kühn, H. Tropical warming in the Timor Sea led deglacial antarctic warming and atmospheric CO_2 rise by more than 500 yr. *Earth and Planetary Science Letters* **302**, 337-348, doi:10.1016/j.epsl.2010. 12.021 (2011).
21. Mudelsee, M. Ramp function regression: A tool for quantifying climate transitions. *Computers and Geosciences* **26**, 293–307 (2000).
22. Kuhnt, W., Blümel, M., Boch, R., Tri Dewi, K., da Costa de Monteiro, F., Dürkop, A., Hanebuth, T., Heidemann, U., Holbourn, A., Jian, Z., van der Kaars, S., Kawamura, H., Kawohl, H., Nürnberg, D., Opdyke, B., Petersen, A., Regenberg, M., Rosenthal, Y., Ruhlemann, C., Sadekov, A., Salomon, B., Tian, J., Xu, J., and Zuraida, R. Variability of the Indonesian Throughflow and Australasian climate history of the last 150 000 years. Cruise Report Sonne-185 VITAL (Darwin-Jakarta September 15 2005 - October 06 2005). http://www.gpi.uni-kiel.de/~wk/SO-185VITAL (2005).
23. Bassinot, F., Baltzer, A., Chen, M.-T., De Deckker, P., Kuhnt, W., Levitan, M., Nürnberg, D., Oba, T., Prentice, M., Sarnthein, M., Situmorang, M., Tiedemann, R., Holbourn, A., Kiefer, T., Pflaumann, U., and Rothe, S. Scientific report of the WEPAMA Cruise MD122/ IMAGES VII. Institut Polaire Français, Paul-Émile Victor (IPEV). Réf: OCE/2002/01 (2002).
24. Hesse, P.P., and McTainsh, G.H. Australian dust deposits: modern processes and the Quaternary record. *Quaternary Science Reviews* **22**, 2007-2035, doi:10.1016/S0277-3791(03)00164-1 (2003).
25. Holbourn, A., Kuhnt, W., Kawamura, H., Jian, Z., Grootes, P., Erlenkeuser, H., and Xu, J. Orbitally paced paleoproductivity variations in the Timor Sea and Indonesian Throughflow variability during the last 460 kyr. *Paleoceanography* **20**, 3002, doi:10.1029/2004PA001094 (2005).